

Measurements of Phase Dynamics in Planar Josephson Junctions and SQUIDs

D. Z. Haxell,¹ E. Cheah,² F. Krizek,^{1,2} R. Schott,² M. F. Ritter,¹ M. Hinderling,¹
W. Belzig,³ C. Bruder,⁴ W. Wegscheider,² H. Riel,¹ and F. Nichele^{1,*}

¹IBM Research Europe - Zurich, Säumerstrasse 4, 8803 Rüschlikon, Switzerland

²Solid State Physics Laboratory, ETH Zurich, 8093 Zurich, Switzerland

³Fachbereich Physik, Universität Konstanz, D-78457 Konstanz, Germany

⁴Department of Physics, University of Basel, Klingelbergstrasse 82, CH-4056 Basel, Switzerland
(Dated: November 22, 2022)

We experimentally investigate the stochastic phase dynamics of planar Josephson junctions (JJs) and superconducting quantum interference devices (SQUIDs) defined in epitaxial InAs/Al heterostructures, and characterized by a large ratio of Josephson energy to charging energy. We observe a crossover from a regime of macroscopic quantum tunneling to one of phase diffusion as a function of temperature, where the transition temperature T^* is gate-tunable. The switching probability distributions are shown to be consistent with a small shunt capacitance and moderate damping, resulting in a switching current which is a small fraction of the critical current. Phase locking between two JJs leads to a difference in switching current between that of a JJ measured in isolation and that of the same JJ measured in an asymmetric SQUID loop. In the case of the loop, T^* is also tuned by a magnetic flux.

Two-dimensional superconductor/semiconductor hybrid systems are a promising platform for scalable quantum computation and for the study of novel physical phenomena. The possibility to produce transparent interfaces [1–9], combined with flexible lithographic patterning, is paving the way to a new generation of voltage-tunable qubit architectures [10–16], with planar Josephson junctions (JJs) and superconducting quantum interference devices (SQUIDs) as core elements. Furthermore, spin-orbit interaction and Zeeman fields enable a rich playground for fundamental physics [17–19], including the realization of topological states of matter [20–25]. In this context, understanding the phase dynamics of hybrid JJs and SQUIDs, which ultimately determine their switching currents, is crucial.

Here we investigate the stochastic phase dynamics of hybrid JJs defined in an InAs/Al planar heterostructure [3]. We show that macroscopic quantum tunneling (MQT) and phase diffusion (PD) are the most relevant phase escape regimes. The low-temperature mean switching current I_M is a small fraction of the critical current I_C , although the Josephson energy E_J is significantly larger than the charging energy E_C . In JJs with small I_C , the suppression of I_M is strong enough that PD dominates at low temperature. Embedding a JJ in an asymmetric SQUID, an approach intensively pursued for realizing topological states [22–25], modifies the phase escape mechanism. Thus, I_M may significantly vary when a JJ is measured in isolation or in a SQUID (by a factor of approximately 2.5, in the present case). The dominant phase-escape mechanism is further tuned via temperature, gate voltages and fluxes threading the SQUID. Contrary to conventional metallic JJs, no indication of thermal phase activation is observed. Characteristic experimental features are reproduced with a Monte Carlo simulation of the phase dynamics. Our results indicate

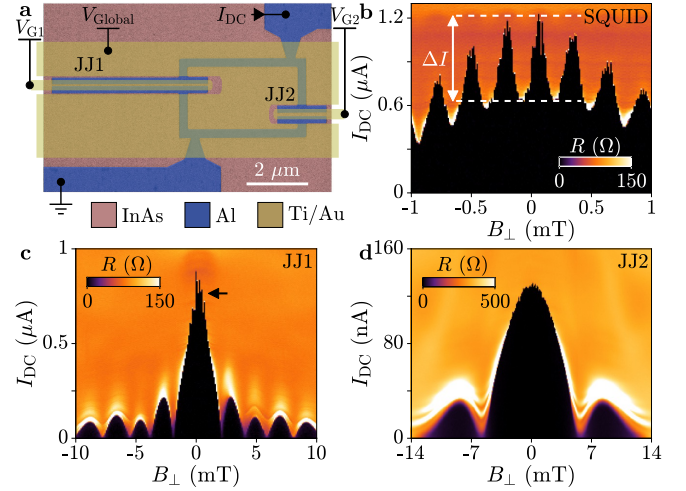


FIG. 1. (a) False-colored electron micrograph of the device under study and measurement configuration. The InAs is highlighted in pink and the Al in blue. Gates are drawn on the image and highlighted in yellow. (b) Differential resistance R as a function of B_{\perp} and I_{DC} obtained with $V_{G1} = -180$ mV and $V_{G2} = -140$ mV. The amplitude of the switching current oscillations, ΔI , is marked. (c) Differential resistance of JJ1 in isolation, with $V_{G1} = -180$ mV and $V_{G2} = -450$ mV. Large fluctuations close to $B_{\perp} = 0$ are marked with an arrow. (d) Differential resistance of JJ2 in isolation, with $V_{G1} = -550$ mV and $V_{G2} = -140$ mV. The peak at $B_{\perp} = 0$ is less than half $\Delta I/2$ in (b).

that phase dynamics significantly affect the switching current of hybrid devices, and guide towards the realization of novel quantum architectures.

Figure 1(a) shows a micrograph of the device under study. It consists of two gate-tunable planar JJs (JJ1 and JJ2) embedded in a SQUID loop, all defined in an InAs quantum well (pink) covered by a thin layer of in-

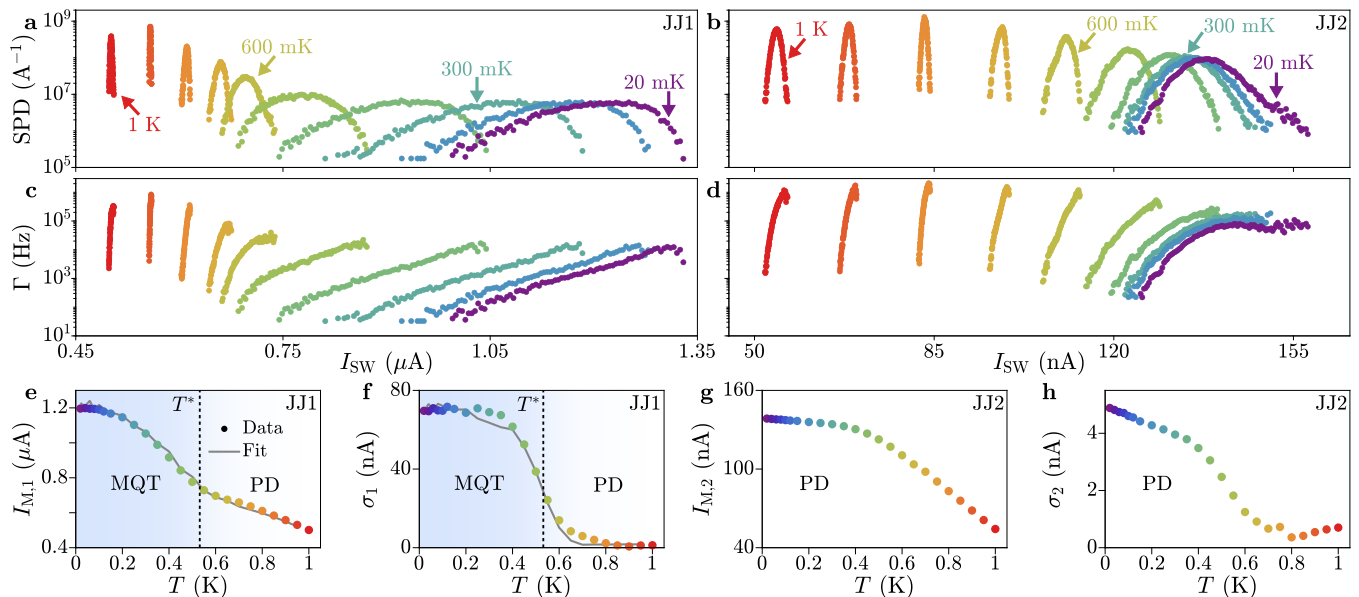


FIG. 2. (a) Switching probability distributions (SPDs) for JJ1 for various temperatures. Colors are defined in (e) and are consistent throughout the text. (b) As in (a), but for JJ2. (c) Escape rate Γ of JJ1, obtained from the data in (a) using Eq. (1). (d) As in (c), but for JJ2. (e) Mean switching current I_{SW} of SPDs for JJ1 as a function of temperature (circles) together with a fit to a Monte Carlo simulation (line). Transition temperature T^* is indicated by a vertical line, dividing a regime of MQT (blue shading) and PD. (f) Standard deviation σ_1 of SPDs for JJ1, as a function of temperature. (g,h) As in (e) and (f), for JJ2.

situ-deposited Al (blue) [3]. Devices were defined by wet etching of the Al, followed by deposition of a 15 nm HfO_x layer and metallic gates (yellow). Gate voltages V_{G1} and V_{G2} allowed tuning of JJ1 and JJ2, respectively. The gate voltage V_{Global} was kept constant at -600 mV to prevent parallel conduction in the semiconductor. The design was optimized to reach a critical current in JJ1 ($I_{C,1}$) that was much larger than the critical current in JJ2 ($I_{C,2}$) [22, 26]. This was achieved by changing the lateral extent of the Al electrodes ($5 \mu\text{m}$ in JJ1 vs. $1.6 \mu\text{m}$ in JJ2) and their separation (50 nm in JJ1 vs. 100 nm in JJ2). Electronic measurements were conducted in a dilution refrigerator with a mixing chamber base temperature below 20 mK. Results presented here were confirmed on a second SQUID device and on several individual JJs.

We first present switching currents obtained with low-frequency lock-in techniques, similar to previous work [18, 22, 26]. A source-drain current I_{DC} was swept over timescales of seconds, while the SQUID differential resistance R was recorded. Figure 1(b) shows R as a function of out-of-plane magnetic field B_{\perp} with $V_{G1} = -180$ mV and $V_{G2} = -140$ mV, where $I_{C,1}$ and $I_{C,2}$ were independently maximized. The SQUID switching current I had a periodicity of $350 \mu\text{T}$, corresponding to a flux $h/2e$ threading the loop. The amplitude of the SQUID oscillations, ΔI , reveals the switching current of JJ2 as $I_2 = \Delta I/2 = 350$ nA, while the mean value gives the switching current of JJ1, $I_1 = 850$ nA. Figure 1(c) shows R when JJ2 is closed and with JJ1 in the gate

configuration of Fig. 1(b). The Fraunhofer interference pattern emerges [27], with a maximum of I_1 matching the mean switching current of Fig. 1(b). Furthermore, large switching current fluctuations were present at $B_{\perp} = 0$ (black arrow). Figure 1(d) shows similar measurements performed with I_{DC} flowing in JJ2 only. Surprisingly, the maximum of I_2 is 120 nA; a significant difference with the 350 nA deduced from Fig. 1(b).

Both the fluctuations in Fig. 1(c) and the switching current enhancement in Fig. 1(b) with respect to Fig. 1(d) are manifestations of the phase dynamics in our devices. Therefore, we evaluate the phase escape mechanisms in JJ1 and JJ2 separately (Fig. 2), and in the SQUID loop formed by their combination (Fig. 3). Finally, we demonstrate gate and flux tunability of the escape dynamics (Fig. 4). To capture the stochastic characteristics of phase escape, we modulate the input current with a sawtooth function using a ramp rate $\nu = 240 \mu\text{As}^{-1}$ and monitor the voltage across the SQUID with an oscilloscope. This technique allows us to record the switching current I_{SW} for 10,000 switching events in approximately ten minutes, and produce the switching probability distribution (SPD), that is the probability for a switch to occur per unit of input current. Similar techniques were used for detailed studies of conventional [28, 29] and hybrid JJs [30–33], metallic nanowires [34–36] and SQUIDs [37–41].

Figures 2(a) and (b) show the SPDs of JJ1 and JJ2, respectively, measured at various mixing chamber temper-

atures T . The corresponding escape rates Γ , computed as [42]

$$\Gamma(I_{\text{SW}}) = \text{SPD}(I_{\text{SW}})\nu \left[1 - \int_0^{I_{\text{SW}}} \text{SPD}(I)dI \right]^{-1}, \quad (1)$$

are shown in Fig. 2(b) and (d), respectively.

Figure 2(e) and (f) show the mean value of the SPDs in JJ1 ($I_{\text{M},1}$) and its standard deviation (σ_1), respectively, both as a function of T . For $T < 400$ mK, σ_1 is constant and large, and Γ increases exponentially with I_{SW} , indicating that MQT dominates the phase dynamics. For higher T , σ_1 decreases as T increases, signaling the crossover to PD, where escape and retrapping events have similar probabilities to occur, so that many escape events are required to transition to the resistive state. The temperature $T^* \sim 0.55$ K marks the crossover between a regime dominated by MQT and one dominated by PD. Regimes with σ_1 increasing with T , which indicate thermal activation (TA), were not observed. The width of the low-temperature SPD, expressed as $\sigma/I_1 = 0.058$, is particularly large and results in pronounced switching current fluctuations, as seen in the measurements of Fig. 1(c) (black arrow). Broad SPDs at low T , together with the absence of an intermediate TA regime, which is unusual in conventional JJs [43], indicate a large critical current $I_{\text{C},1}$ and a small capacitance C for JJ1. Finally, the relevance of PD, together with measuring a finite resistance at $I_{\text{DC}} = 0$ for $T > 1$ K, which is well below the critical temperature T_{C} of the Al [44], indicates moderate damping.

The temperature dependence of $I_{\text{M},1}$ and σ_1 is well captured by a Monte Carlo simulation of the phase dynamics [gray line in Figs. 2(e,f)] [45], an approach previously adopted for the study of moderately damped JJs [46, 47]. In particular, the capacitance C and the zero-temperature critical current $I_{\text{C},1}$ of JJ1 are first obtained by comparing the low-temperature data to a model of MQT. The quality factor Q_0 is subsequently determined by comparing the full temperature dependence to the Monte Carlo simulation. Details on our procedure are discussed in the Supplemental Material [44]. While this model was developed for tunneling JJs with sinusoidal current-phase relation and large Q_0 , in the absence of a more complete theory, we tentatively apply it to our devices and consider the results to be of qualitative nature. The best fit was obtained with $C = 1$ fF, $I_{\text{C},1} = 3 \mu\text{A}$ and $Q_0 = 7$. As expected, JJ1 is moderately damped and has a small intrinsic capacitance, leading to a large plasma frequency. The estimated $I_{\text{C},1}$ is 2.5 times higher than $I_{\text{M},1}$, indicating that moderate input currents already result in a high switching probability. The ratio between $I_{\text{C},1}$ and $I_{\text{M},1}$ decreases towards one for $T > T^*$, as signaled by the kink in $I_{\text{M},1}$ at $T = T^*$. The result $C = 1$ fF is consistent with the geometrical capacitance between the Al electrodes [44]. With these

parameters, we estimate $E_{\text{J}}/E_{\text{C}} = 73$ at $T = 20$ mK [44]. This situation is very different from conventional metallic Josephson junction, where strong suppression of I_{SW} from I_{C} requires $E_{\text{J}}/E_{\text{C}} \leq 1$ [48–50]. Due to the small C and large I_{C} , we estimate that the transition from MQT to TA would occur for $T > T_{\text{C}}$ so that, in the entire PD regime, phase escape takes place via MQT [44].

Similar to JJ1, MQT is the dominant phase escape mechanism in JJ2. However, large dissipation results in a significant retrapping probability and places JJ2 in the PD regime down to base temperature. This is evident from $I_{\text{M},2}$ and σ_2 shown in Figs. 2(g) and (h), respectively, where σ_2 does not saturate for $T \rightarrow 0$, and from the deviation of Γ from an exponential in Fig. 2(d). The small $I_{\text{C},2}$ likely sets $Q_0 \sim 1$, which is outside the range of validity of our Monte Carlo simulations.

We now present the phase dynamics when both JJs are activated. Figures 3(a) and (b) show the mean, $I_{\text{M},\text{S}}$, and standard deviation, σ_{S} , of each SPD obtained in the gate configuration of Fig. 1(b) as a function of B_{\perp} and T [51]. In Fig. 3(a), SQUID oscillations are clearly captured by $I_{\text{M},\text{S}}$. In Fig. 3(b), the curves at low T have a large σ_{S} , independent of B_{\perp} . As T increases further, σ_{S} is modulated by B_{\perp} and ultimately becomes small and independent of B_{\perp} . In Fig. 3(c) we compare $I_{\text{M},2}$ [squares, as in Fig. 2(g)] to the half-amplitude of the oscillations in $I_{\text{M},\text{S}}$ (circles). In the absence of macroscopic quantum tunneling, the two quantities would coincide. Instead, we find a significant discrepancy, highlighted by green shading, which is large at low T and vanishes above T^* of JJ1. By tuning T^* via $V_{\text{G}1}$, we confirm that the enhancement of $\Delta I_{\text{M},\text{S}}/2$ with respect to $I_{\text{M},2}$ was always correlated to T^* in JJ1 [44]. The mean value of $I_{\text{M},\text{S}}$ matched $I_{\text{M},1}$ [44] and the mean of σ_{S} , $\langle \sigma_{\text{S}} \rangle$, was similar to σ_1 [Fig. 3(d)].

The results presented in Fig. 3 are intuitively understood by considering phase-locking by the loop inductance. For JJ2 alone, phase escape is more likely at moderate currents compared to JJ1. Coupling JJ2 to JJ1 effectively realizes a new JJ with higher Josephson energy and similar phase dynamics to JJ1, so that the dominant switching mechanism is MQT and, consequently, the suppression of I_{M} is reduced. However, protection of $I_{\text{M},2}$ is maintained while JJ1 stays in the MQT regime ($T < T^*$), where phase uncertainty is less than in the PD regime. Consistent with this interpretation, phase dynamics in the asymmetric SQUID configuration are well described by a Monte Carlo simulation of a fictitious JJ with a field-dependent critical current $I_{\text{C},\text{S}}(B_{\perp})$, and with C and Q_0 as derived for JJ1. The sole fit parameter was $I_{\text{C},\text{S}}$ for $T = 20$ mK, which is shown in Fig. 3(e) as a function of B_{\perp} (circles). The curve is consistent with the presence of highly-transmissive Andreev bound states (ABSSs), resulting in a forward-skewed current-phase relation [26, 52]. Also for the SQUID, critical current $I_{\text{C},\text{S}}$ and mean switching current $I_{\text{M},\text{S}}$ [Fig. 3(a)] differ by a factor of approximately 2.5. After obtaining $I_{\text{C},\text{S}}(B_{\perp})$

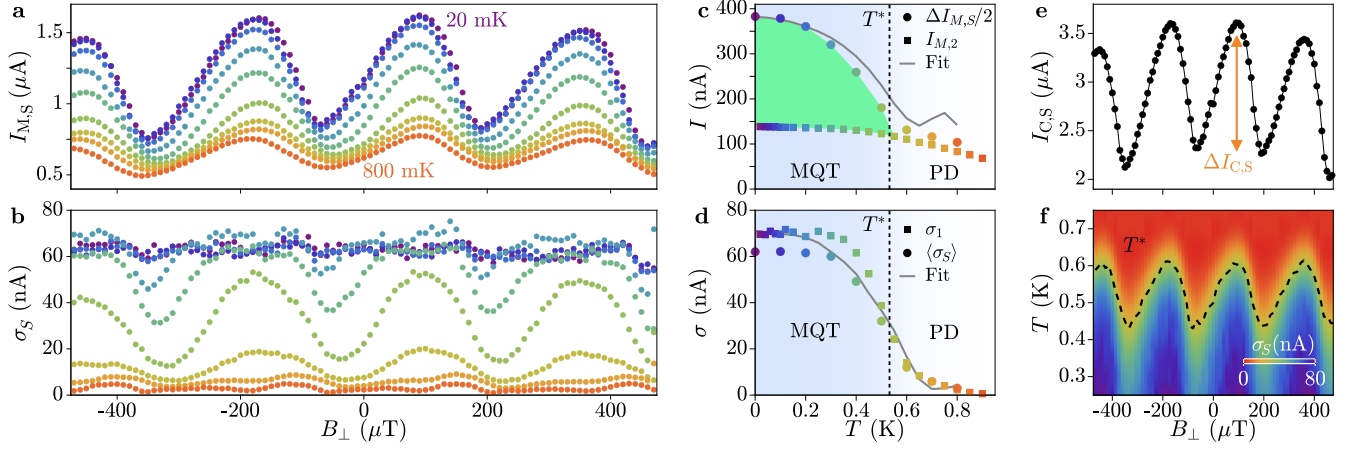


FIG. 3. Mean $I_{M,S}$ (a) and standard deviation σ_S (b) of the SPDs in the SQUID configuration as a function of B_{\perp} , for temperatures between 20 and 800 mK. (c) Mean switching current of JJ2 as a function of T , derived from the SQUID oscillations (circles) and measured with JJ2 in isolation (squares). The solid line is $\Delta I_{M,S}/2$ obtained from a Monte Carlo simulation fitted to the experimental results. (d) Standard deviation of the SPD in JJ1 measured in isolation (squares) together with the mean of σ_S from (b) (circles) as a function of temperature. The solid line is the result of the Monte Carlo simulation presented in (c). (e) SQUID critical current obtained by fitting the SPDs for $T = 20$ mK to an MQT escape rate. (f) Color map of fitted standard deviation σ_S , with transition temperature T^* marked by a dashed line.

for $T = 20$ mK, the entire dataset of Figs. 3(a) and (b) was simulated without free parameters. We show the simulated half-amplitude $\Delta I_{M,S}/2$ and the mean of σ_S as gray lines in Figs. 3(c) and (d) respectively. Despite the simplicity of our model, experimental results are reproduced to a large extent. Figure 3(f) shows a colormap of the simulated standard deviation, $\sigma_S(B_{\perp}, T)$, with T^* indicated by a dashed line and marking the crossover between MQT and PD. The phase dynamics are completely described by MQT and PD for low and high T , respectively. For intermediate T , the phase escape mechanism periodically varies between MQT and PD as a function of B_{\perp} .

In the following, we discuss how phase escape dynamics vary as $I_{C,1}$ and $I_{C,2}$ are tuned via gate voltages. Figure 4(a) summarizes results for JJ2 as V_{G2} was varied. When JJ2 was measured in isolation, switching currents $I_{M,2}$ were small and PD was the dominant regime throughout the accessible range of V_{G2} . We highlight this condition with gray shading. When the SQUID was formed, the switching current of JJ2 deduced from the SQUID oscillations ($\Delta I_{C,S}/2$) was significantly higher than when JJ2 was measured in isolation. We highlight this situation with green shading. For $V_{G2} < 300$ mV JJ2 was resistive, if measured in isolation, presumably due to $E_J/E_C \approx 1$ [48–50], but SQUID oscillations were still observed. Finally, the $I_{C,2}$ obtained by fitting the SPDs in the SQUID with the Monte Carlo simulation [as in Fig. 3(e)] is highlighted in yellow.

Decreasing $I_{C,1}$ via V_{G1} made the SQUID more symmetric and shifted JJ1 towards a regime of PD. Figures 4(b-d) show σ_S for decreasing values of V_{G1} . For $V_{G1} = -300$ mV and -350 mV (Figs. 4(c) and (d), re-

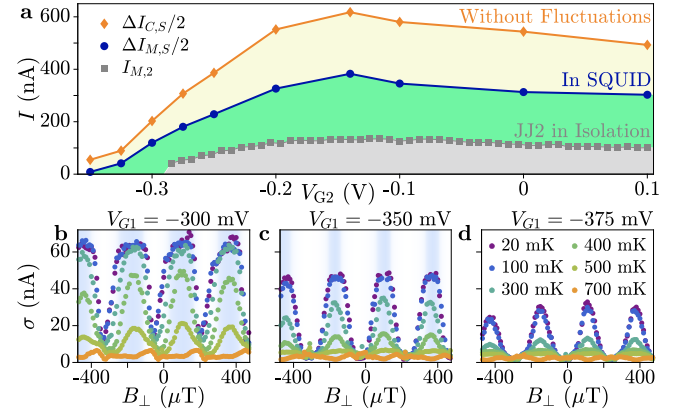


FIG. 4. (a) Switching currents of JJ2 as a function of V_{G2} when measured in isolation (squares) and in the SQUID configuration (circles), together with the critical current derived from Monte Carlo simulations (diamonds). (b-d) Standard deviation of SPDs measured in the SQUID configuration for three values of V_{G1} . Blue shading highlights MQT regimes.

spectively) escape dynamics varied between MQT (blue shading) and PD already at base temperature, with σ_S oscillating between 10 and 60 nA within one SQUID oscillation. For $V_{G1} = -375$ mV [Fig. 4(d)] PD dominated at low T , although modulations in σ_S persisted. Modeling the curves in Figs. 4(b-d) would require a quantum treatment of the phase escape from a 2D potential, which goes beyond the scope of this work.

In conclusion, the switching current of planar JJs with highly transmissive ABSs is strongly affected by phase dynamics, even for $E_J/E_C \gg 1$. As a result of moderate dissipation ($Q_0 < 10$) and large plasma frequency, I_M

can differ largely from I_C , depending on the details of the JJs and of their electrostatic environment. Phase dynamics can be modified by embedding JJs in asymmetric SQUID geometries, resulting in significant changes of I_M . Furthermore, the dominant phase-escape mechanism in a SQUID can be tuned between MQT and PD via a magnetic flux, affecting the SQUID switching current and its standard deviation. This intricate physics is relevant for realizing gate-tunable quantum devices and investigating topological phenomena, where hybrid JJs with phase control are widespread.

We are grateful to C. Müller and W. Riess for helpful discussions. We thank the Cleanroom Operations Team of the Binnig and Rohrer Nanotechnology Center (BRNC) for their help and support. F. N. acknowledges support from the European Research Council (grant number 804273) and the Swiss National Science Foundation (grant number 200021.201082). W. B. acknowledges support from the European Union's Horizon 2020 FET Open programme (grant number 964398) and from the Deutsche Forschungsgemeinschaft (DFG; German Research Foundation) via the SFB 1432 (ID 425217212).

* fni@zurich.ibm.com

- [1] P. Krogstrup, N. L. B. Ziino, W. Chang, S. M. Albrecht, M. H. Madsen, E. Johnson, J. Nygård, C. Marcus, and T. S. Jespersen, *Nature Materials* **14**, 400 (2015).
- [2] W. Chang, S. M. Albrecht, T. S. Jespersen, F. Kuemmeth, P. Krogstrup, J. Nygård, and C. M. Marcus, *Nature Nanotechnology* **10**, 232 (2015).
- [3] J. Shabani, M. Kjaergaard, H. J. Suominen, Y. Kim, F. Nichele, K. Pakrouski, T. Stankevic, R. M. Lutchyn, P. Krogstrup, R. Feidenhans'l, S. Kraemer, C. Nayak, M. Troyer, C. M. Marcus, and C. J. Palmstrøm, *Phys. Rev. B* **93**, 155402 (2016).
- [4] F. Vigneau, R. Mizokuchi, D. C. Zanuz, X. Huang, S. Tan, R. Maurand, S. Frolov, A. Sammak, G. Scappucci, F. Lefloch, and S. De Franceschi, *Nano Lett.* **19**, 1023 (2019).
- [5] C. M. Moehle, C. T. Ke, Q. Wang, C. Thomas, D. Xiao, S. Karwal, M. Lodari, V. van de Kerkhof, R. Termaat, G. C. Gardner, G. Scappucci, M. J. Manfra, and S. Goswami, *Nano Lett.* **21**, 9990 (2021).
- [6] P. Perla, H. A. Fonseka, P. Zellekens, R. Deacon, Y. Han, J. Kölzer, T. Mörstedt, B. Bennemann, A. Espiari, K. Ishibashi, D. Grützmacher, A. M. Sanchez, M. I. Lepsa, and T. Schäpers, *Nanoscale Adv.* **3**, 1413 (2021).
- [7] T. Kanne, M. Marnauza, D. Olsteins, D. J. Carrad, J. E. Sestoft, J. de Bruijckere, L. Zeng, E. Johnson, E. Olsson, K. Grove-Rasmussen, and J. Nygård, *Nature Nanotechnology* **16**, 776 (2021).
- [8] M. Pendharkar, B. Zhang, H. Wu, A. Zarassi, P. Zhang, C. P. Dempsey, J. S. Lee, S. D. Harrington, G. Badawy, S. Gazibegovic, R. L. M. Op het Veld, M. Rossi, J. Jung, A.-H. Chen, M. A. Verheijen, M. Hocevar, E. P. A. M. Bakkers, C. J. Palmstrøm, and S. M. Frolov, *Science* **372**, 508 (2021).
- [9] K. Aggarwal, A. Hofmann, D. Jirovec, I. Prieto, A. Sammak, M. Botifoll, S. Martí-Sánchez, M. Veldhorst, J. Arbiol, G. Scappucci, J. Danon, and G. Katsaros, *Phys. Rev. Research* **3**, L022005 (2021).
- [10] T. W. Larsen, K. D. Petersson, F. Kuemmeth, T. S. Jespersen, P. Krogstrup, J. Nygård, and C. M. Marcus, *Phys. Rev. Lett.* **115**, 127001 (2015).
- [11] L. Casparis, M. R. Connolly, M. Kjaergaard, N. J. Pearson, A. Kringhøj, T. W. Larsen, F. Kuemmeth, T. Wang, C. Thomas, S. Gronin, G. C. Gardner, M. J. Manfra, C. M. Marcus, and K. D. Petersson, *Nature Nanotechnology* **13**, 915 (2018).
- [12] C. Janvier, L. Tosi, L. Bretheau, Ç. Girit, M. Stern, P. Bertet, P. Joyez, D. Vion, D. Esteve, M. Goffman, *et al.*, *Science* **349**, 1199 (2015).
- [13] G. de Lange, B. van Heck, A. Bruno, D. J. van Woerkom, A. Geresdi, S. R. Plissard, E. P. A. M. Bakkers, A. R. Akhmerov, and L. DiCarlo, *Phys. Rev. Lett.* **115**, 127002 (2015).
- [14] M. Pita-Vidal, A. Bargerbos, C.-K. Yang, D. J. van Woerkom, W. Pfaff, N. Haider, P. Krogstrup, L. P. Kouwenhoven, G. de Lange, and A. Kou, *Phys. Rev. Applied* **14**, 064038 (2020).
- [15] J. I.-J. Wang, D. Rodan-Legrain, L. Bretheau, D. L. Campbell, B. Kannan, D. Kim, M. Kjaergaard, P. Krantz, G. O. Samach, F. Yan, J. L. Yoder, K. Watanabe, T. Taniguchi, T. P. Orlando, S. Gustavsson, P. Jarillo-Herrero, and W. D. Oliver, *Nature Nanotechnology* **14**, 120 (2019).
- [16] M. Hays, V. Fatemi, D. Bouman, J. Cerrillo, S. Diamond, K. Serniak, T. Connolly, P. Krogstrup, J. Nygård, A. L. Yeyati, A. Geresdi, and M. H. Devoret, *Science* **373**, 430 (2021).
- [17] S. Hart, H. Ren, M. Kosowsky, G. Ben-Shach, P. Leubner, C. Brüne, H. Buhmann, L. W. Molenkamp, B. I. Halperin, and A. Yacoby, *Nature Physics* **13**, 87 (2017).
- [18] W. Mayer, M. C. Dartiailh, J. Yuan, K. S. Wickramasinghe, E. Rossi, and J. Shabani, *Nature Communications* **11**, 212 (2020).
- [19] C. Baumgartner, L. Fuchs, A. Costa, S. Reinhardt, S. Gronin, G. C. Gardner, T. Lindemann, M. J. Manfra, P. E. Faria Junior, D. Kochan, J. Fabian, N. Paradiso, and C. Strunk, *Nature Nanotechnology* **17**, 39 (2022).
- [20] M. Hell, M. Leijnse, and K. Flensberg, *Phys. Rev. Lett.* **118**, 107701 (2017).
- [21] F. Pientka, A. Keselman, E. Berg, A. Yacoby, A. Stern, and B. I. Halperin, *Phys. Rev. X* **7**, 021032 (2017).
- [22] A. Fornieri, A. M. Whiticar, F. Setiawan, E. Portolés, A. C. C. Drachmann, A. Keselman, S. Gronin, C. Thomas, T. Wang, R. Kallagher, G. C. Gardner, E. Berg, M. J. Manfra, A. Stern, C. M. Marcus, and F. Nichele, *Nature* **569**, 89 (2019).
- [23] H. Ren, F. Pientka, S. Hart, A. T. Pierce, M. Kosowsky, L. Lunczer, R. Schlereth, B. Scharf, E. M. Hankiewicz, L. W. Molenkamp, B. I. Halperin, and A. Yacoby, *Nature* **569**, 93 (2019).
- [24] M. C. Dartiailh, W. Mayer, J. Yuan, K. S. Wickramasinghe, A. Matos-Abiague, I. Žutić, and J. Shabani, *Phys. Rev. Lett.* **126**, 036802 (2021).
- [25] A. Banerjee, O. Lesser, M. A. Rahman, H. R. Wang, M. R. Li, A. Kringhøj, A. M. Whiticar, A. C. C. Drachmann, C. Thomas, T. Wang, M. J. Manfra, E. Berg, Y. Oreg, A. Stern, and C. M. Marcus, *Signatures of a*

- topological phase transition in a planar Josephson junction (2022), arXiv:2201.03453 [cond-mat.mes-hall].
- [26] F. Nichele, E. Portolés, A. Fornieri, A. M. Whiticar, A. C. C. Drachmann, S. Gronin, T. Wang, G. C. Gardner, C. Thomas, A. T. Hatke, M. J. Manfra, and C. M. Marcus, *Phys. Rev. Lett.* **124**, 226801 (2020).
- [27] H. J. Suominen, J. Danon, M. Kjaergaard, K. Flensberg, J. Shabani, C. J. Palmstrøm, F. Nichele, and C. M. Marcus, *Phys. Rev. B* **95**, 035307 (2017).
- [28] T. A. Fulton and L. N. Dunkleberger, *Phys. Rev. B* **9**, 4760 (1974).
- [29] J. M. Martinis, M. H. Devoret, and J. Clarke, *Phys. Rev. B* **35**, 4682 (1987).
- [30] G.-H. Lee, D. Jeong, J.-H. Choi, Y.-J. Doh, and H.-J. Lee, *Phys. Rev. Lett.* **107**, 146605 (2011).
- [31] A. Murphy, P. Weinberg, T. Aref, U. C. Coskun, V. Vakaryuk, A. Levchenko, and A. Bezryadin, *Phys. Rev. Lett.* **110**, 247001 (2013).
- [32] B.-K. Kim and Y.-J. Doh, *Journal of the Korean Physical Society* **69**, 349 (2016).
- [33] J. Kim, B.-K. Kim, H.-S. Kim, A. Hwang, B. Kim, and Y.-J. Doh, *Nano Lett.* **17**, 6997 (2017).
- [34] M. Sahu, M.-H. Bae, A. Rogachev, D. Pekker, T.-C. Wei, N. Shah, P. M. Goldbart, and A. Bezryadin, *Nature Physics* **5**, 503 (2009).
- [35] P. Li, P. M. Wu, Y. Bomze, I. V. Borzenets, G. Finkelstein, and A. M. Chang, *Phys. Rev. Lett.* **107**, 137004 (2011).
- [36] T. Aref, A. Levchenko, V. Vakaryuk, and A. Bezryadin, *Phys. Rev. B* **86**, 024507 (2012).
- [37] V. Lefevre-Seguin, E. Turlot, C. Urbina, D. Esteve, and M. H. Devoret, *Phys. Rev. B* **46**, 5507 (1992).
- [38] S.-X. Li, Y. Yu, Y. Zhang, W. Qiu, S. Han, and Z. Wang, *Phys. Rev. Lett.* **89**, 098301 (2002).
- [39] F. Balestro, J. Claudon, J. P. Pekola, and O. Buisson, *Phys. Rev. Lett.* **91**, 158301 (2003).
- [40] D. F. Sullivan, S. K. Dutta, M. Dreyer, M. A. Gubrud, A. Roychowdhury, J. R. Anderson, C. J. Lobb, and F. C. Wellstood, *Journal of Applied Physics* **113**, 183905 (2013), <https://doi.org/10.1063/1.4804057>.
- [41] S. Butz, A. K. Feofanov, K. G. Fedorov, H. Rotzinger, A. U. Thomann, B. Mackrodt, R. Dolata, V. B. Geshkenbein, G. Blatter, and A. V. Ustinov, *Phys. Rev. Lett.* **113**, 247005 (2014).
- [42] A. Bezryadin, Stochastic premature switching and Kurkijärvi theory, in *Superconductivity in Nanowires* (John Wiley & Sons, Ltd, 2012) Chap. 8, pp. 131–162.
- [43] L. Longobardi, D. Massarotti, D. Stornaiuolo, L. Galletti, G. Rotoli, F. Lombardi, and F. Tafuri, *Phys. Rev. Lett.* **109**, 050601 (2012).
- [44] See the Supplemental Material at [URL] for a detailed discussion of the Monte Carlo simulation and for additional experimental results.
- [45] J. C. Fenton and P. A. Warburton, *Phys. Rev. B* **78**, 054526 (2008).
- [46] L. Longobardi, D. Massarotti, G. Rotoli, D. Stornaiuolo, G. Papari, A. Kawakami, G. Piero Pepe, A. Barone, and F. Tafuri, *Appl. Phys. Lett.* **99**, 062510 (2011).
- [47] L. Longobardi, D. Massarotti, G. Rotoli, D. Stornaiuolo, G. Papari, A. Kawakami, G. P. Pepe, A. Barone, and F. Tafuri, *Phys. Rev. B* **84**, 184504 (2011).
- [48] J. M. Martinis and R. L. Kautz, *Phys. Rev. Lett.* **63**, 1507 (1989).
- [49] M. Iansiti, A. T. Johnson, W. F. Smith, H. Rogalla, C. J. Lobb, and M. Tinkham, *Phys. Rev. Lett.* **59**, 489 (1987).
- [50] M. Iansiti, M. Tinkham, A. T. Johnson, W. F. Smith, and C. J. Lobb, *Phys. Rev. B* **39**, 6465 (1989).
- [51] Each SPD was obtained by recording 5,000 switching events.
- [52] C. W. J. Beenakker and H. van Houten, *Phys. Rev. Lett.* **66**, 3056 (1991).
- [53] D. Massarotti, L. Longobardi, L. Galletti, D. Stornaiuolo, D. Montemurro, G. Pepe, G. Rotoli, A. Barone, and F. Tafuri, *Low Temperature Physics* **38**, 263 (2012), <https://doi.org/10.1063/1.3699625>.
- [54] C. R. Paul, *Analysis of Multiconductor Transmission Lines* (Wiley-IEEE Press).
- [55] M. H. Devoret, J. M. Martinis, and J. Clarke, **55**, 1908.
- [56] R. L. Kautz and J. M. Martinis, **42**, 9903.
- [57] K. Gloos and F. Anders, **116**, 21.
- [58] A. A. Golubov, M. Y. Kupriyanov, and E. Il'ichev, **76**, 411.

SUPPLEMENTAL MATERIAL

Sample Fabrication

Samples were fabricated from a heterostructure grown on InP (001) substrates by molecular beam epitaxy techniques. The heterostructure consists of a step-graded metamorphic InAlAs buffer and a 7 nm thick InAs quantum well, confined by $\text{In}_{0.75}\text{Ga}_{0.25}\text{As}$ barriers 10 nm below the surface. A 10 nm thick Al layer is deposited on top of the heterostructure, in the same chamber as the III-V growth while maintaining vacuum. The peak mobility is $18000 \text{ cm}^2\text{V}^{-1}\text{s}^{-1}$ for an electron density of $n = 8 \cdot 10^{11} \text{ cm}^{-2}$. This gives an electron mean free path of $l_e \gtrsim 350 \text{ nm}$, hence we expect all JJs measured here to be ballistic along the length L of the junction.

The sample is defined by first isolating the large mesa structures on which the device is patterned. This is done by selectively removing the top Al layer (with Al etchant Transene D) before etching $\sim 250 \text{ nm}$ into the III-V heterostructure using a chemical wet etch ($220 : 55 : 3 : 3$ solution of $\text{H}_2\text{O} : \text{C}_6\text{H}_8\text{O}_7 : \text{H}_3\text{PO}_4 : \text{H}_2\text{O}_2$). The Al device is then patterned on top of the mesa, by selective etching of the Al with Transene D at $50 \text{ }^\circ\text{C}$ for 4 s. To control the exposed III-V region, we deposit a 15 nm layer of HfO_2 by atomic layer deposition, before evaporating metallic gate electrodes. These are deposited in two steps: the first consists of 5 nm Ti and 20 nm of Au on top of the device region; the second, 10 nm of Ti and 350 nm of Al, contacts the gates on top of the mesa to the bonding pads.

Lock-in Measurements

Electrical measurements were performed in a dilution refrigerator with a mixing chamber temperature below 20 mK. Initial characterization was performed by standard lock-in techniques. An AC current of $I_{\text{AC}} = 2 \text{ nA}$ was applied to the source contact of the SQUID device, with a frequency of 233 Hz. The four-terminal differential voltage V_{AC} across the SQUID was measured at this frequency, via a differential voltage amplifier with 1000 times gain. The differential resistance $R = V_{\text{AC}}/I_{\text{AC}}$ was measured as a function of the applied DC current I_{DC} .

In addition to the B_{\perp} -dependent measurements presented in Fig. 1 of the Main Text, we show temperature- and gate-dependent measurements of JJ1 and JJ2. In Figs. S.1(a) and (b), for JJ1 and JJ2 respectively, we show the differential resistance R as a function of I_{DC} , swept from negative to positive currents. The color denotes the temperature, which ranges from 20 mK to 1.6 K, at which point both JJs are fully resistive. We offset the vertical axis by $200 \text{ } \Omega$ between each temperature trace, to highlight the zero-resistance state at low bias currents.

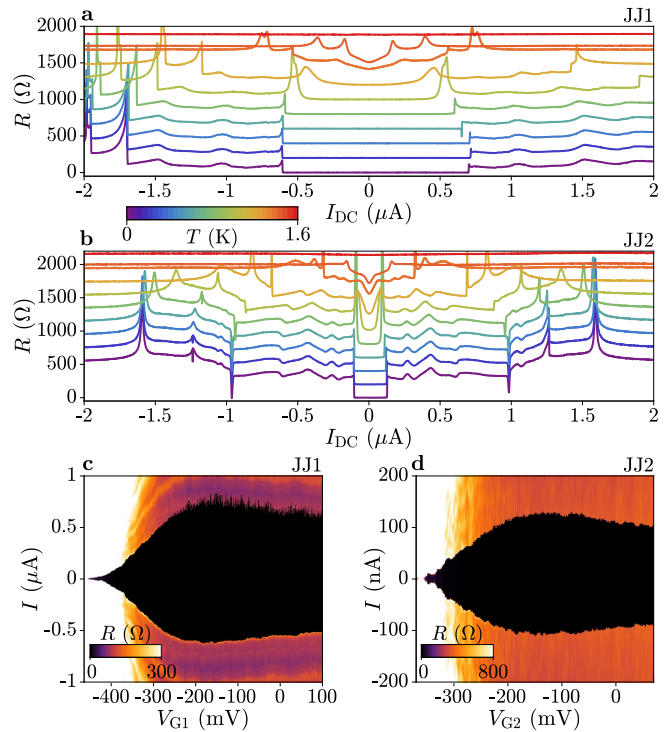


FIG. S.1. (a) Current-biased measurement of differential resistance R of JJ1 with an applied bias of I_{DC} , in the positive sweep direction. (b) Same as (a) for JJ2. (c) Differential resistance R of JJ1 as a function of gate voltage V_{G1} . The junction goes from fully open to fully closed in the gate voltage range. (d) Same as (c) for JJ2. Note that the color scale in (c) and (d) is saturated to highlight the normal state resistance R_N close to zero gate voltage.

As we increase I_{DC} from $-2 \text{ } \mu\text{A}$, each junction undergoes a transition from the resistive to superconducting state at the retrapping current I_{R} . At positive bias, the superconducting-to-resistive transition occurs at the switching current I_{SW} . The difference between the two, most notable in JJ1, indicates the underdamped JJ behavior. At high temperatures the superconducting state softens, leading to a finite resistance at bias values below I_{SW} . This is expected from phase diffusive JJs at high temperatures, but makes determination of I_{SW} less reliable; hence we do not present SPDs at temperatures $T > 1 \text{ K}$, where this effect is significant.

Figures S.1(c) and (d) show the gate dependence of the differential resistance R across JJ1 and JJ2, respectively. The normal state resistances for JJ1 and JJ2 are $R_{\text{N},1} = 150 \text{ } \Omega$ and $R_{\text{N},2} = 540 \text{ } \Omega$, respectively. At a small negative gate voltage, the switching current reaches its maximum. The peak occurs at $V_{\text{G1}} = -180 \text{ mV}$ for JJ1 and $V_{\text{G2}} = -140 \text{ mV}$ for JJ2. These define the operating points for each junction in Figs. 1-3 of the Main Text. Each JJ can be tuned to the completely resistive state with sufficiently negative gate voltages,

as seen in Figs. S.1(c) and (d) for JJ1 and JJ2 respectively. To measure a single junction in isolation, we apply $V_G < -400$ mV to the other junction so that no super-current flows there, as in Figs. 1,2 of the Main Text. In Fig. S.1(c), we observe large fluctuations in the switching current for $V_{G1} > -200$ mV. This is indicative of large quantum fluctuations when the critical current is large.

Phase Escape in Single JJs

Phase dynamics in Josephson junctions are often described using the analogy of a massive phase particle in a tilted washboard potential, where the particle mass corresponds to the JJ capacitance and its damping to the inverse of its resistance. The zero-resistance state corresponds to the particle being trapped in an energy minimum while the resistive state corresponds to the particle moving along the potential. A transition to the resistive state generally takes place, via quantum or thermal fluctuations, at switching currents I_{SW} lower than the JJ critical current I_C . To measure this transition, we apply a sawtooth signal from a waveform generator through a bias resistor to rapidly ramp I_{DC} , and detect a switch to the resistive state by measuring the point at which the voltage across the JJ increases above a threshold. The value of I_{DC} at which this switch occurs is recorded as the switching current, I_{SW} . We measure I_{SW} more than 10,000 times and collect the results in a switching probability distribution (SPD). The SPDs are recorded as a function of temperature, from 20 mK to 1 K.

The SPDs are dependent on the rate at which the DC current is increased, ν . To compare with theoretical expressions for phase dynamic mechanisms, we must convert to a measurement-independent quantity: the escape rate, Γ . This is done via KFD transform using the following equation [42]:

$$\Gamma(I_{SW}) = \text{SPD}(I_{SW})\nu \left[1 - \int_0^{I_{SW}} \text{SPD}(I)dI \right]^{-1} \quad (\text{S.1})$$

where ν is the ramp rate of the DC current, which was $\nu = 240 \mu\text{As}^{-1}$ for all measurements.

In the following, we will consider equations derived for JJs with a sinusoidal current-phase relation. While our JJs are known to contain highly-transmissive modes, leading to deviations from this sinusoidal behavior, we use the existing theory in the absence of an alternative model and expect only small numerical deviation from the results presented.

The rate of escape of a Josephson junction to the resistive state under the action of a DC bias follows the general dependence [53]:

$$\Gamma(I_{SW}, T) = \Omega(I_{SW}, T)e^{-\Delta U(I_{SW}, T)/k_B T}, \quad (\text{S.2})$$

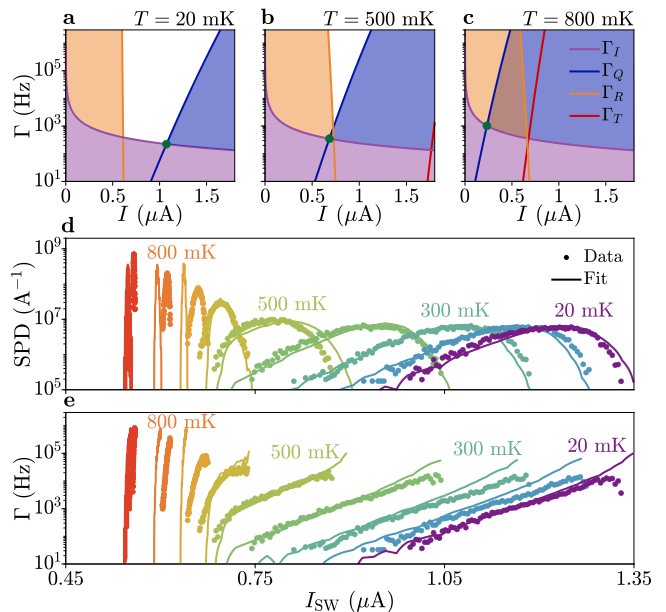


FIG. S.2. (a-c) Simulated escape rates for $T = 20$ mK, 500 mK and 800 mK respectively, for the fit parameters of JJ1. Bias-current ramp-rate Γ_I , MQT escape rate Γ_Q , re-trapping rate Γ_R and thermal escape rate Γ_T are compared across the bias range I . The green dot indicates $\Gamma_I = \Gamma_Q$, at which point escape events are measurable. (d) SPDs of JJ1: Experimental data (points) compared with Monte Carlo simulation (lines) for temperatures 20 mK to 1 K. The temperature is indicated by the color, as in the Main Text. (e) Escape rates corresponding to the SPDs in (d).

where Ω is the attempt frequency and ΔU is the potential barrier height. Under a reduced DC bias of $\gamma = I_{DC}/I_C$, the approximate barrier height is $\Delta U = 2E_J \left(\sqrt{1 - \gamma^2} - \gamma \cos^{-1} \gamma \right)$, with a Josephson energy of $E_J = \hbar I_C / 2e$.

A transition to the resistive state can be promoted, for currents lower than I_C , by macroscopic quantum tunnelling (MQT) or thermal activation (TA) across the barrier ΔU . In the case of MQT, equation S.1 is adjusted to the analytical formula for escape [53]

$$\Gamma_Q = \frac{\omega_P}{2\pi} \sqrt{\frac{864\pi\Delta U}{\hbar\omega_P}} \exp\left(-7.2 \left(1 + \frac{0.87}{Q}\right) \frac{\Delta U}{\hbar\omega_P}\right), \quad (\text{S.3})$$

where $\omega_P = \omega_{P0} (1 - \gamma^2)^{1/4}$ is the plasma frequency at γ and Q is the quality factor of the junction. The junction capacitance C enters in the bare plasma frequency, $\omega_{P0} = \sqrt{2eI_C/\hbar C}$.

When dissipation is large it is possible for the junction to transition from the resistive to the superconducting state, referred to as re-trapping. In this regime, many escape events are required to turn the junction resistive. This is referred to as phase diffusion (PD). For $Q \gg 1$, we can use an analytical formula for this re-trapping rate

[53]:

$$\Gamma_R = \frac{I_{SW} - I_R}{I_C} \omega_{P0} \sqrt{\frac{E_J}{2\pi k_B T}} \exp\left(-\left(\frac{I_{SW} - I_R}{I_C}\right)^2 \frac{E_J Q^2}{2k_B T}\right) \quad (\text{S.4})$$

where I_R is the retrapping current. We measure intermediately damped junctions with $Q \gtrsim 1$, so this relation can only be considered as an approximation.

The interplay between Γ_Q and Γ_R determines the phase escape regime: $\Gamma_Q \gg \Gamma_R$ in the MQT regime, whereas the reverse is true for phase diffusion. The rates depend on the junction properties: the critical current I_C , the capacitance C and the quality factor, which has the zero-temperature value Q_0 . We show in Figs. S.2(a-c) the relevant rates in the system for the fit parameters for JJ1: $I_C = 3 \mu\text{A}$, $C = 1 \text{ fF}$ and $Q_0 = 7$, as discussed in more detail later. Each panel corresponds to a different temperature: $T = 20 \text{ mK}$, $T = 500 \text{ mK}$ and $T = 800 \text{ mK}$, respectively. These highlight the change in the dominant regime from MQT to PD on increasing T .

The ramp rate $\Gamma_I(I) = \nu/I$ defines the lowest frequencies at which an escape event can be measured, for a given bias current I . The point at which this intersects the escape rate gives the lowest bias current I_{IE} at which an escape event is measurable. Since quantum tunneling is the dominant escape mechanism, we define I_{IE} as the current at which $\Gamma_I = \Gamma_Q$, marked in Figs. S.2(a-c) with the green dot. The retrapping rate Γ_R is large for low bias currents but quickly decreases with an increase in I . Retrapping is significant when Γ_R reaches a similar magnitude as Γ_Q . Escape by thermal activation is given by Γ_T , and is much smaller than Γ_Q for all temperatures.

At the lowest temperature, escape by quantum tunneling dominates. This is clear since $\Gamma_Q \gg \Gamma_R$ for $I > I_{IE}$. No retrapping of the phase occurs: a single escape event is sufficient to transition to the resistive state. At $T = 500 \text{ mK}$, $\Gamma_Q \lesssim \Gamma_R$ close to I_{IE} . For these low bias currents, the retrapping probability is high so the probability of escape in the junction is reduced relative to quantum tunneling alone. However, $\Gamma_Q \gg \Gamma_R$ at larger bias so escape occurs unhindered by phase diffusion. As the temperature increases, the effect of retrapping becomes more significant. At the high temperature of 800 mK , phase diffusion is dominant since $\Gamma_Q \ll \Gamma_R$ across the range of escape currents.

The transition temperature T^* between MQT and PD regimes is experimentally defined as the inflection point of the standard deviation as a function of temperature. This is the point at which the retrapping rate Γ_R becomes dominant above MQT escape Γ_Q . We can specify this further as the temperature at which the escape, retrapping and ramp rates are equal, T_{IER}^* . This is similar to Ref. [45]. The trend of I_M with temperature, for the single junctions and the SQUID, changes at T^* (see Figs. 2(e) and 3(c) in the Main Text). This suggests that our definition of T^* is appropriate as a measure of the

transition between MQT and PD regimes.

The rates in Figs. S.2(a-c) are used to model the junction behavior in a Monte Carlo simulation, as in Ref. [45]. As the DC bias current is increased, the simulated junction stochastically switches between the superconducting (0) and resistive (1) states according to the relative escape and retrapping rates. The junction is said to be resistive when the state, averaged over a window of current, exceeds 0.1. This process is performed 20,000 times and the generated I_{SW} are combined into a switching probability distribution (SPD).

The simulation uses the critical current I_C , capacitance C and quality factor Q_0 as input parameters for the rates Γ_Q and Γ_R . We fit by hand the SPD at low temperature, obtaining $I_C = 3 \mu\text{A}$, $C = 1 \text{ fF}$ and $Q_0 = 7$. We use the Bardeen formula for the temperature dependence of $I_C(T) = I_C(1 - T^2/T_C^2)^{3/2}$, with $T_C = 1.18 \text{ K}$ from experimental results. Since $Q \propto I_C^{1/2}$, we use $Q(T) = Q_0(1 - T^2/T_C^2)^{3/4}$. We use the low-temperature fit result and the assumed temperature dependence to simulate the full dataset. Figures S.2(d) and (e) show the SPDs and escape rates for JJ1, respectively. The experimental data (circles) is fitted well by the simulated curve (lines). Deviation at high temperatures between the fit and the data is explained by the simple model used for the temperature dependence. Despite this, we capture the characteristic trend in the data.

We now consider the impact of temperature on the switching current in the MQT regime. In Fig. S.3 we calculate the SPD as a function of temperature using the same fit parameters as Fig. S.2, but considering only MQT escape without the presence of PD ($\Gamma_R = 0$). This is instructive to see the impact of the temperature dependence of I_C and Q on SPDs at low T . In particular, we see that the mean switching current $I_{M,1}$ decreases with increasing temperature [Fig. S.3(a)]. This is due to the low T_C of Al, which causes a change in I_C even at the lowest temperature of our experiment. This is evident in Fig. S.3(b) (dashed line). The experimental data for $I_{M,1}$ (squares) aligns with the simulated result for MQT in the absence of PD (solid line) up to $T \sim T^*$. This is indicative of the dominance of MQT over PD up to $T \sim T^*$ in the experimental data. In Fig. S.3(c) we show the experimental standard deviation σ_1 (squares) and the modelled standard deviation in the case of pure MQT (line). The slight temperature dependence of the fit result is due to the temperature dependence of Q , again a consequence of the low T_C in Al.

Further to the standard deviation, as shown in the Main Text, the skewness of SPDs is indicative of the phase escape mechanism. Phase escape unhindered by retrapping leads to a negative skewness close to -1 [31]. On entering the PD regime, the SPDs become more symmetric and the skewness tends towards zero. This is shown in Figs. S.4(a-c), where SPDs of JJ1 are plotted on a

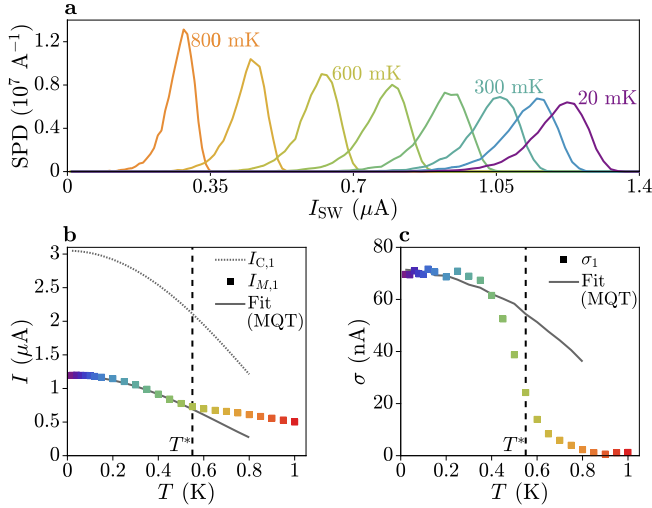


FIG. S.3. (a) Switching probability distributions (SPDs) obtained from a Monte Carlo simulation considering only escape by quantum tunneling (MQT), as a function of temperature. Calculated using the parameters $I_C = 3 \mu\text{A}$, $C = 1 \text{ fF}$ and $Q_0 = 7$. (b) Temperature dependence of critical current $I_{C,1}$ (dashed line), JJ1 switching current $I_{M,1}$ (squares) and MQT-only fit (solid line). (c) Temperature dependence of standard deviation in JJ1 (squares) and MQT-only fit (line).

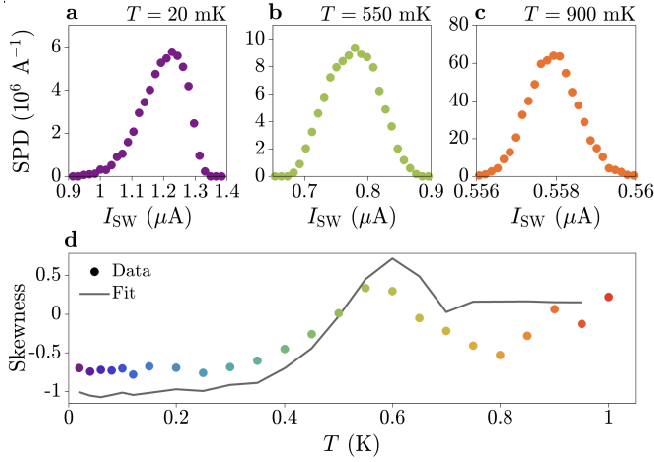


FIG. S.4. (a) Switching probability distribution (SPD) of JJ1 at $T = 20 \text{ mK}$, plotted on a linear scale. Large negative skewness, consistent with a lack of phase diffusion at low temperature. (b) SPD at $T = 550 \text{ mK}$, where skewness is positive. (c) Symmetric SPD at $T = 900 \text{ mK}$. (d) Skewness of SPDs (circles) as a function of temperature, as indicated by the color. This is compared with the result from the Monte Carlo fit (gray curve).

linear scale for $T = 20 \text{ mK}$, 550 mK and 900 mK respectively. The trend in skewness is consistent with the interpretation above. At low temperature the SPD has large negative skewness, indicating that no phase diffusion is present. At higher temperatures, the SPDs are more symmetric with a skewness of zero at $T = 900 \text{ mK}$.

The skewness of JJ1 as a function of temperature (circles) is plotted in Fig. S.4(d), alongside the Monte Carlo fit result (gray line). Both the data and the Monte Carlo fit are negative at low temperature, and increase towards zero for higher temperatures where phase diffusion becomes dominant.

In general, the quality factor of the junction is described by $Q = RC\omega_P$. For $I_C = 3 \mu\text{A}$ and $C = 1 \text{ fF}$ we get a resistance of $R = 2.33 \text{ k}\Omega$, much larger than the normal state resistance at low frequency of $R_{N,1} = 150 \Omega$. We therefore conclude that damping at high frequency is relevant in the case of these junctions. For $Q \gg 1$, we can relate the quality factor to the ratio of critical and re-trapping currents: $Q = 4I_C/\pi I_R$. For JJ1, $I_R = 600 \text{ nA}$ giving $Q = 6.4$, close to the fit value.

Escape by quantum tunneling is dominant up to the critical temperature. By comparing Eqs. S.2 and S.3, we obtain an effective temperature of quantum tunneling escape,

$$k_B T_Q = \frac{\hbar\omega_P}{7.2(1 + 0.87/Q)}. \quad (\text{S.5})$$

At low temperature, $T_Q \approx 3 \text{ K}$ for JJ1. This exemplifies the large scale of quantum fluctuations relative to thermal excitations. The temperature at which $T_Q < T$ for the parameters of JJ1 is approximately 1 K : thermal activation is not significant up to the critical temperature.

Estimation of the Geometrical Capacitance

The capacitance $C = 1 \text{ fF}$ obtained in the Monte Carlo simulation is consistent with the geometrical capacitance of JJ1, calculated as the coplanar capacitance between epitaxial Al electrodes and given by the formula [54]:

$$C = \frac{\epsilon_0 \epsilon_r W}{\pi} \ln \left[-2 \left(\frac{\beta + 1}{\beta - 1} \right) \right], \quad (\text{S.6})$$

where $\beta = \sqrt[4]{1 - \frac{L^2}{(L+2L_S)^2}}$. We use the dielectric constant $\epsilon_r = 12.3$ of InAs at high frequency. The geometrical parameters of the junction are: lateral extent of JJ electrodes, $W = 5 \mu\text{m}$; separation of JJ electrodes, $L = 40 \text{ nm}$; and length of superconducting leads, $L_S = 250 \text{ nm}$. This gives $C = 1.4 \text{ fF}$. The calculation does not consider the effect of the top gate electrode, which is grounded via a low-impedance terminal. It therefore acts as a screening layer for the electric field between the two junction electrodes. This reduces the capacitance, up to a factor of 2 for complete screening of half of the field between the Al electrodes. The presence of JJ2 in the SQUID loop contributes an additional shunt capacitance of $C_2 = 0.2 \text{ fF}$, for junction parameters $W_2 = 1.6 \mu\text{m}$, $L_2 = 100 \text{ nm}$ and $L_{S,2} = 250 \text{ nm}$. Screening of the field by the electrostatic gates may reduce this by up to a factor of 2. The contribution of JJ2

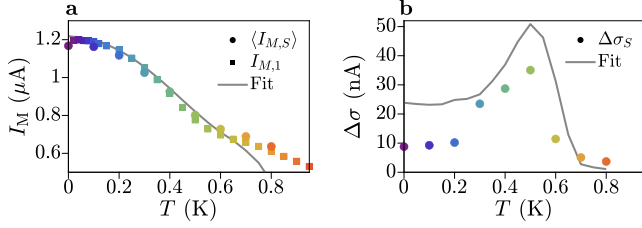


FIG. S.5. (a) Average value of $I_{M,S}$ across B_{\perp} (circles), as a function of temperature (as indicated by the color), compared with the mean switching current of JJ1 in isolation $I_{M,1}$ (squares) and a fit obtained by Monte Carlo simulation (gray curve). (b) Difference between the maximal and minimal σ_S across B_{\perp} , $\Delta\sigma_S$ (circles), which indicates the size of the field-dependence in σ_S at a given temperature. This is compared with a Monte Carlo simulation (gray line), which reproduces the trend.

to the capacitance of JJ1 is therefore small, and does not modify the conclusions of the Main Text.

The large leads of the device might contribute as well to the shunt capacitance. Their geometrical capacitance, calculated with Eq. S.6, is about 3 fF. This value is likely decreased by the presence of the large gate electrodes between them. This analysis does not consider shunt capacitances present in the bonding pads and in the wiring of the dilution refrigerator. The extent to which shunt capacitances contributes to the plasma frequency is an open question, investigated in Refs. [55–57]. The interpretation in the Main Text of a planar Josephson junction with a small capacitance C is supported by the result of an analytical fit to Eq. S.3, a Monte Carlo simulation of the temperature dependence, a consideration of the geometrical capacitance of the junction and a comparison to values previously reported in literature [18, 30].

Full SQUID Data and Monte Carlo Simulation

Figure 3 in the Main Text shows the switching probability in the SQUID configuration, as a function of B_{\perp} and T . From $I_{M,S}$ and σ_S as a function of B_{\perp} we extract $\Delta I_{M,S}/2$ and $\langle\sigma_S\rangle$. In Fig. S.5, we plot the remaining extracted parameters $\langle I_{M,S}\rangle$ and $\Delta\sigma_S$ (circles) with the corresponding results for the Monte Carlo simulation (lines).

Figure S.5(a) shows the field-averaged value of the oscillations in $I_{M,S}$ (circles) compared with $I_{M,1}$, the mean switching current for JJ1 (squares). The two align across all temperatures, confirming that JJ1 dominates the average SQUID behavior.

The Monte Carlo simulation (gray line) follows the data at low temperatures, but some deviations emerge above $T = 600$ mK when the junction is almost completely phase diffusive. The escape rates are particularly sensitive to the damping Q in this regime, so deviations

between simulations and experiment at high temperature might be accounted for with a more complex temperature dependence. Figure 3(c) of the Main Text shows a similar deviation in $\Delta I_{M,S}/2$, most likely from the same effect.

We observe a strong magnetic-field-dependence of the standard deviation in the SQUID, which is characterized by $\Delta\sigma_S$ in Fig. S.5(b). Close to the transition temperature $T^* \approx 0.55$ K, $\Delta\sigma_S$ is more than 35 nA. Both at low and high temperature, σ_S is almost constant across magnetic field. Oscillations in the simulated σ_S (gray lines) were observed at low-temperature, contrary to the experimental data, hence the larger simulated $\Delta\sigma_S$.

The results are compared with the Monte Carlo simulation (lines). As described in the Main Text, the fit parameter $I_{C,S}$ is obtained from the low-temperature data. Since the SQUID is in the MQT regime, we fit each escape rate with Eq. S.3 using a fixed $C = 1$ fF and $Q_0 = 7$ from JJ1. The skewness of $I_{C,S}$ indicates that highly transmissive modes are present in the junction. To capture this skewness, we consider a JJ with many modes of equal transmission $\bar{\tau}$:

$$I_{C,S} = I_{C,1} + I_0 \frac{\sin(\varphi)}{\sqrt{1 - \bar{\tau} \sin^2(\varphi/2)}}, \quad (\text{S.7})$$

with $I_{C,1} = 3 \mu\text{A}$, $I_0 = 480$ nA and effective transmission $\bar{\tau} = 0.77$. This gives $\Delta I_{C,S}/2 = 650$ nA. The mean value of $I_{C,S}$ at $T = 20$ mK is given by the solid line in Fig. S.5(a). We use the low-temperature result to simulate the full dataset by varying $I_{C,1}$ and I_0 with a Bardeen dependence, as for the isolated junctions.

We can further quantify the properties of JJ1 and JJ2 by considering their $I_C R_N$ product [58]. This gives $I_{C,1} \cdot R_{N,1} = 3 \mu\text{A} \cdot 150 \Omega = 450 \mu\text{V}$ and $I_{C,2} \cdot R_{N,2} = 650 \text{ nA} \cdot 540 \Omega = 350 \mu\text{V}$, for JJ1 and JJ2 respectively. The expected $I_C R_N$ product is $\pi\Delta/e$ in the clean limit, or $\pi\Delta/2e$ in the tunneling limit ($l_e < \xi$). For a superconducting gap of $\Delta = 180 \mu\text{eV}$, this gives $I_C R_N = 565 \mu\text{V}$ or $283 \mu\text{V}$, respectively. Hence, both JJ1 and JJ2 are in an intermediate regime between the clean and tunneling limits, with JJ2 closer to the tunneling limit than JJ1.

V_{G2} Dependence

In an asymmetric SQUID, the amplitude of oscillations as a function of B_{\perp} is an indication of the current flowing through the small junction. This is an approximation to

$$I_{C,S} = \sqrt{(I_{C,1} - I_{C,2})^2 + 4I_{C,1}I_{C,2} \cos^2\left(\frac{\varphi - \varphi_0}{2}\right)}, \quad (\text{S.7})$$

when $I_{C,1} \gg I_{C,2}$. We use this equation to extract the critical current of JJ2 in the asymmetric SQUID, as a function of gate voltage V_{G2} .

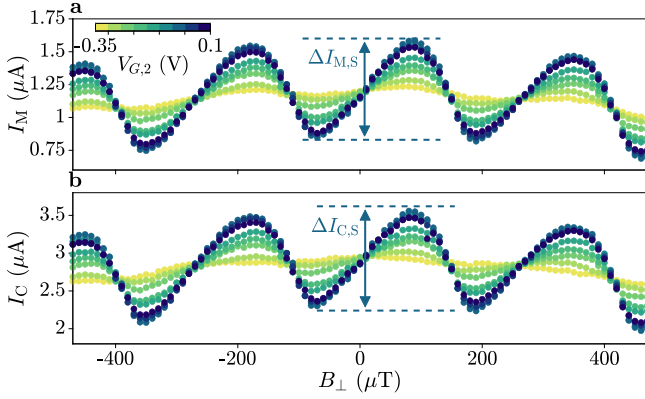


FIG. S.6. (a) Mean switching current $I_{M,S}$ as a function of B_{\perp} , taken at $T = 20$ mK for different values of the JJ2 gate voltage, V_{G2} . The oscillation amplitude $\Delta I_{M,S}/2$ gives the switching current of JJ2 in the SQUID, as indicated by the arrow for $V_{G2} = -100$ mV. (b) Critical current $I_{C,S}$, obtained from the curves in (a) by fitting SPDs in the MQT regime. The oscillation amplitude $I_{C,2} = \Delta I_{C,S}/2$ gives the critical current of JJ2 as a function of V_{G2} , as indicated by the arrow for $V_{G2} = -100$ mV

We measure SQUID oscillations at $T = 20$ mK and fixed $V_{G1} = -180$ mV, with different V_{G2} [see Fig. S.6(a)]. The SQUID is always in the MQT regime, independent of V_{G2} , and the asymmetry is large. For each V_{G2} , we extract $\Delta I_{M,S}/2$ as shown, and plot the results in Fig. 4(a) of the Main Text. We extract the critical current $I_{C,S}$ by fitting each SPD with Eq. S.3 in the MQT regime, with fixed capacitance C and quality factor Q_0 defined by JJ1. The result is shown in Fig. S.6(b), from which we extract $I_{C,2} = \Delta I_{C,S}/2$.

V_{G1} Dependence

We tune the phase dynamics of JJ1 with a gate voltage V_{G1} . We measure SPDs for JJ1 as a function of temperature at gate voltages spanning the range of critical currents. In Fig. S.7(a,b) we plot the mean and standard deviation of SPDs, respectively. As V_{G1} is tuned to more negative values, the transition temperature T^* decreases until $V_{G1} = -400$ mV, where JJ1 is fully phase diffusive at the lowest temperature in the measurement. This transition is clear from both the mean switching current $I_{M,1}$ and standard deviation σ_1 . At $V_{G1} = -320$ mV, σ_1 at $T = 20$ mK is 50 nA, reduced relative to 65 nA at $V_{G1} = -180$ mV. Additionally, σ_1 is not constant with temperature even down to the lowest measured value of T . Finally, the kink in $I_{M,1}$ and the inflection point in σ_1 occur at $T^* \approx 0.4$ K. These features all indicate a stronger relevance of PD, such that it is present at 20 mK and becomes dominant at a lower temperature: T^* is decreased.

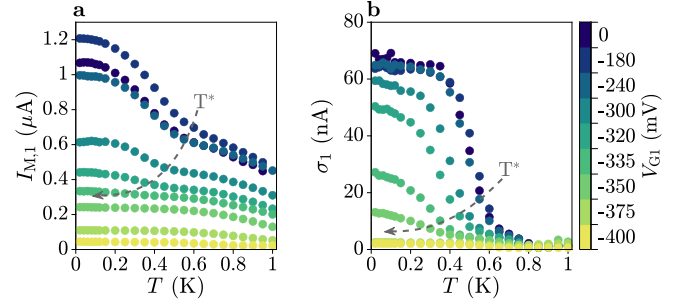


FIG. S.7. (a) Mean switching current $I_{M,1}$ of switching probability distributions (SPDs) of JJ1 as a function of temperature. Measured for different gate voltages V_{G1} , as indicated by the color. The decrease in transition temperature T^* with V_{G1} is indicated by the arrow. (b) Standard deviation σ_1 of SPDs of JJ1 as a function of temperature, for different gate voltages V_{G1} . The decrease in T^* with V_{G1} is indicated by the arrow.

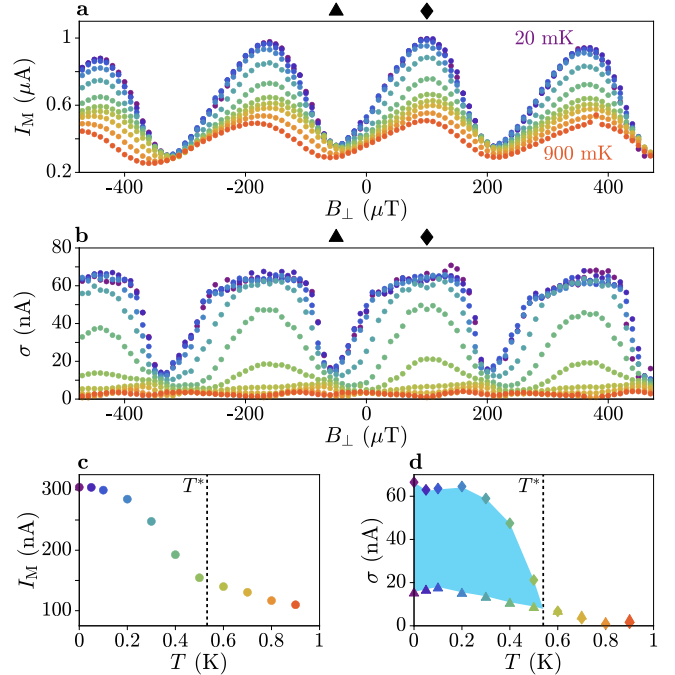


FIG. S.8. (a) Mean switching current $I_{M,S}$ for the SQUID configuration $V_{G1} = -300$ mV and $V_{G2} = -140$ mV, as a function of B_{\perp} . Field traces are taken at temperatures ranging from 20 mK up to 900 mK. The maximum (diamond) and minimum (triangle) of the $I_{M,S}$ oscillations are marked. (b) Standard deviation σ_S in this SQUID configuration, for temperatures 20 mK to 900 mK. (c) Oscillation amplitude of $I_{M,S}$, $\Delta I_{M,S}/2$ as a function of temperature. A kink in $\Delta I_{M,S}/2$ occurs at the transition temperature of $T^* \approx 0.52$ K. (d) Standard deviation σ_S at values of B_{\perp} corresponding to the $I_{M,S}$ maximum (diamonds) and minimum (triangles) respectively. The large difference at $T < T^*$ is indicated.

The regime of the SQUID is dominated by JJ1, the large I_C component, so we can change the SQUID behavior by varying V_{G1} . For $V_{G1} = -300$ mV, the SQUID undergoes direct transitions between MQT and PD depending on B_{\perp} [Fig. 4(b) in the Main Text]. The full dataset is shown in Fig. S.8 for 20 mK to 900 mK: the mean switching current $I_{M,S}$ in (a) and the standard deviation in (b).

The oscillation amplitude $\Delta I_{M,S}/2$ is shown in Fig. S.8(c). The enhancement in switching current at low temperatures is again observed, where quantum tunneling is dominant. We also observe the characteristic kink in $\Delta I_{M,S}/2$, in this case at $T \approx 0.52$ K concomitant with the lower transition temperature to the phase diffusive regime.

At $T = 20$ mK, we observe a large variation in the standard deviation σ_S depending on the field B_{\perp} . At the maximum of $I_{M,S}$ (diamond), σ_S is large at low temperature. This is consistent with quantum tunneling as the dominant mechanism of phase escape. Instead, $\sigma_S = 20$ nA at the minimum (triangle), indicating that phase diffusive effects are strong. The traces in σ_S at these field values are shown in Fig. S.8(d) by their respective markers. The large difference in σ_S is evident at low temperatures, as indicated by the blue shading, where the external magnetic field determines the extent of phase diffusion in the SQUID. On increasing T towards the transition temperature, the difference in σ_S reduces until the SQUID is fully phase-diffusive at all values of B_{\perp} .

Figures S.9 and S.10 show the datasets for $V_{G1} = -350$ mV and $V_{G1} = -375$ mV, respectively. While still asymmetric for $V_{G1} = -350$ mV, the critical current of JJ1 is no longer much larger than that of JJ2. The much lower critical current of JJ1 means that quantum tunneling is only dominant close to the maximum of the SQUID oscillations. This is highlighted in Fig. S.9(b). At the minima, the SQUID is fully phase diffusive with $\sigma_S < 5$ nA. The oscillation amplitude $\Delta I_{M,S}/2$ in Fig. S.9(c) shows a kink at $T \approx 0.42$ K, which is consistent with the average transition temperature between MQT and PD regimes. Figure S.9(d) shows σ_S at flux values corresponding to the maximum (diamonds) and minimum (triangles) of the $I_{M,S}$ oscillations. The divergence for $T < T^*$ is evident, as in Fig. S.8(d). We note that at some values of B_{\perp} in the low-temperature curve the switching current went above the signal amplitude, artificially truncating the SPD and rendering its standard deviation unphysical: these points have been

removed from the trace.

On further decrease in V_{G1} to -375 mV, the SQUID is almost symmetric. In this case, a magnetic-field dependence is still observable in the standard deviation [see Fig. S.10(b)] but the SQUID is phase diffusive at $T = 20$ mK for all values of B_{\perp} . The corresponding oscillation amplitude, while no longer representative of

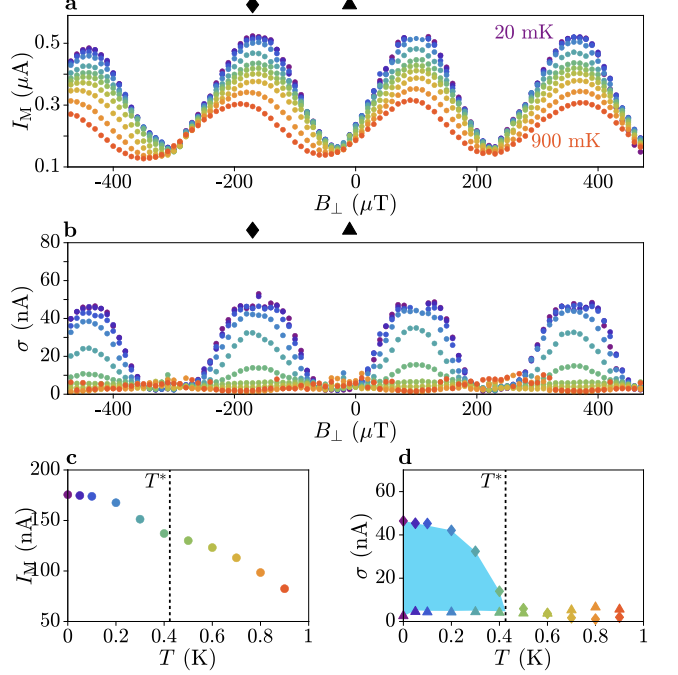


FIG. S.9. (a) Mean switching current $I_{M,S}$ for the SQUID configuration $V_{G1} = -350$ mV and $V_{G2} = -140$ mV, as a function of B_{\perp} . Field traces are taken at temperatures ranging from 20 mK up to 900 mK. The maximum (diamond) and minimum (triangle) of the $I_{M,S}$ oscillations are marked. (b) Standard deviation σ_S in this SQUID configuration, for temperatures 20 mK to 900 mK. (c) Oscillation amplitude of $I_{M,S}$, $\Delta I_{M,S}/2$ as a function of temperature. A kink in $\Delta I_{M,S}/2$ occurs at the transition temperature of $T^* \approx 0.42$ K. (d) Standard deviation σ_S at values of B_{\perp} corresponding to the $I_{M,S}$ maximum (diamonds) and minimum (triangles) respectively. The large difference at $T < T^*$ is indicated.

the switching current of JJ2, again shows the kink in $\Delta I_{M,S}/2$ at the low transition temperature of $T \approx 0.35$ K. Figure S.10(d) shows σ_S at the maxima (diamonds) and minima (triangles) of $I_{M,S}$, and while some divergence emerges for $T < T^*$, phase diffusion is dominant for all values of B_{\perp} .

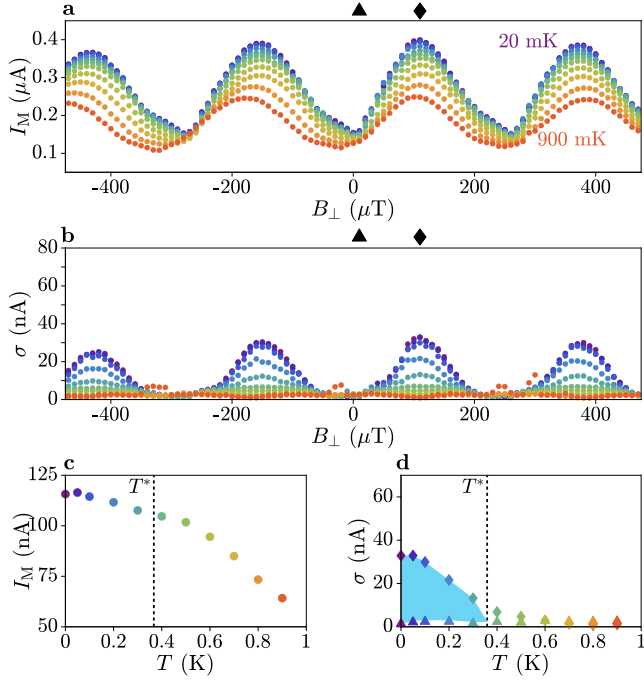


FIG. S.10. (a) Mean switching current $I_{M,S}$ for the SQUID configuration $V_{G1} = -375$ mV and $V_{G2} = -140$ mV, as a function of B_\perp . Field traces are taken at temperatures ranging from 20 mK up to 900 mK. The maximum (diamond) and minimum (triangle) of the $I_{M,S}$ oscillations are marked. (b) Standard deviation σ_S in this SQUID configuration, for temperatures 20 mK to 900 mK. (c) Oscillation amplitude of $I_{M,S}$, $\Delta I_{M,S}/2$ as a function of temperature. A kink in $\Delta I_{M,S}/2$ occurs at the transition temperature of $T^* \approx 0.35$ K. (d) Standard deviation σ_S at values of B_\perp corresponding to the $I_{M,S}$ maximum (diamonds) and minimum (triangles) respectively. The large difference at $T < T^*$ is indicated.